**Geomechanics and Engineering**, *Vol. 32, No. 6 (2023) 639-652*
https://doi.org/10.12989/gae.2023.32.6.639


# 3D stability of pile stabilized stepped slopes considering seismic and surcharge loads

Long Wang[1,3,4], Meijuan Xu*[2,3], Wei Hu[4], Zehang Qian[5] and Qiujing Pan[5]

[1]*School of Environment and Civil Engineering, Jiangnan University, Wuxi 214122, China*
[2]*Mechanical Engineering Department, Zhejiang University City College, Hangzhou 310015, Zhejiang, China*
[3]*Guangxi Key Laboratory of Disaster Prevention and Engineering Safety, Key Laboratory of Disaster Prevention and Structural Safety of Ministry of Education, College of Civil Engineering and Architecture, Guangxi University, Nanning 530004, China*
[4]*State Key Laboratory of Geohazard Prevention and Geoenvironmental Protection, Chengdu University of Technology, Chengdu 610059, China*
[5]*Department of Civil Engineering, Central South University, Changsha 410075, China*

(*Received July 13, 2021, Revised February 21, 2023, Accepted February 23, 2023*)

**Abstract.** Stepped earth slopes incorporated with anti-slide piles are widely utilized in landslide disaster preventions. Explicit consideration of the three-dimensional (3D) effect in the slope design warrants producing more realistic solutions. A 3D limit analysis of the stability of pile stabilized stepped slopes is performed in light of the kinematic limit analysis theorem. The influences of seismic excitation and surcharge load are both considered from a kinematic perspective. The upper bound solution to the factor of safety is optimized and compared with published solutions, demonstrating the capability and applicability of the proposed method. Comparative studies are performed with respect to the roles of 3D effect, pile location, pile spacing, seismic and surcharge loads in the safety assessments of stepped slopes. The results demonstrate that the stability of pile reinforced stepped slopes differ with that of single stage slopes dramatically. The optimum pile location lies in the upper portion of the slope around $L_x/L$ = 0.9, but may also lies in the shoulder of the bench. The pile reinforcement reaches 10% universally for a looser pile spacing $D_c/d_p$ = 5.0, and approaches 70% when the pile spacing reaches $D_c/d_p$ = 2.0.

**Keywords:** limit analysis; pile; pseudo-static method; safety factor; slope stability

## 1. Introduction

Stepped slopes, for their advantages in improving the slope stability, are commonly encountered in engineering projects, such as embankments and unsupported excavations (Li *et al*. 2020). By a rational selection of the bench width and the slope configuration, such as convex and concave shapes (Sun *et al*. 2017), or incorporated with the reinforcement techniques, such as retaining walls and anti-slide piles (Ersoy *et al*. 2020, Liu *et al*. 2020, Son *et al*. 2021), a safe and economic design can usually be achieved. In engineering practice, though the slope failures exhibit evident 3D features, they are usually treated two-dimensionally with the most adverse cross-sections being concerned. It is widely recognized that, compared with the 3D solutions, the 2D ones are usually conservative in both the slope safety estimations (Ersoy *et al*. 2020, Gonzalez *et al*. 2020) and the back analyses of soil shear strength parameters (Stark and Eid 1998). Therefore, an explicit consideration of the 3D effect warrants producing more realistic results and is critical for a safe and economic design of the stepped earth slopes.

3D approaches for slope stability estimations are usually developed directly from the 2D ones, and the solutions are mainly based on the limit-equilibrium theorem, the numerical techniques, or the limit analysis method. Though the limit-equilibrium method is not rigorous in the sense of mechanics and some nonnegligible limitations exist (Pan *et al*. 2021), it remains the most classical approach in the stability problems of earthworks and numerous findings have been reported by many scholars (e.g., Lam and Fredlund 1993, Deng *et al*. 2017, Liu *et al*. 2019, Liu *et al*. 2020). Limit analysis has also been proved to be an efficient method to estimate the limit load acting on geostructures. Employing the upper- and lower-bound theorems, the true solutions can be bracketed in a range of ± 10% (Lim *et al*. 2015). 3D limit analysis method arises from the 2D ones and becomes a hot topic in recent years. In the development of 3D limit analysis method, a variety of admissible failure mechanisms have been reported and boost the utilization of this method in slope stability analyses greatly (e.g., Michalowski and Drescher 2009, Gao *et al*. 2015, Deng *et al.* 2019, Rao *et al*. 2020, Zheng *et al*. 2020, Pang *et al*. 2020, Park *et al*. 2021, Zhao *et al*. 2020), especially for unsaturated soils (Chen *et al*. 2021, 2023, Wang *et al*. 2019, 2020, 2021a, b, 2023, Hong *et al*. 2023).

Anti-slide piles are widely adopted to maintain the stability of natural or man-made slopes that are considered to be unstable. By a rational design of the pile-related parameters (e.g., pile location, spacing, diameter and embedment depth), the slope safety can be improved to a desired value. In the safety assessments of pile reinforced

*Corresponding author, Professor
E-mail: xumeijuannj@163.com



ISSN: 2005-307X (Print), 2092-6219 (Online)

slopes, the solutions are mostly generated based on the plane strain assumptions (e.g., Deng *et al*. 2017, Zhong *et al*. 2019, Hajiazizi and Heydari 2019). 3D limit-equilibrium analyses of pile reinforced earth slopes are not common.

This is due to the fact that the pile resistance due to soil lateral earth pressure in a 3D version, as well as the pile-soil interaction, can hardly be accounted for based on the limit-equilibrium theorem. Incorporation of the limit-equilibrium method with the finite element technique (Liu *et al*. 2020) might be a promising way for the issued problems. 3D kinematic limit analyses of pile stabilized slopes can be found in the literatures (Gao *et al*. 2015, He *et al*. 2015, Rao *et al*. 2020), but these analyses are limited to single stage slopes. For stepped earth slopes reinforced with a row of anti-slide piles, 3D kinematic limit analyses are not common and the results are relatively rare.

In the framework of limit analysis, this paper investigated the stability of pile stabilized stepped earth slopes and considered the impacts of seismic excitation and surcharge load. The focus of this study lies in the explication of: i.) the differences between 2D and 3D methods, ii.) the influences of slope shapes and pile-related parameters on stepped slope stability, and iii) the impacts of seismic and surcharge loads on the stability pile stabilized slopes. A large number of numerical experiments was carried out to elucidate the role of surcharge load, seismic action and slope configuration in the stability evaluations of pile reinforced stepped slopes.

## 2. Problem description

### 2.1 3D kinematic limit analysis of stepped slopes

In present analysis, a stepped slope in homogeneous frictional and cohesive soil characterized with a bench. The slope height is $H$ and the bench width is $\lambda H$ with $\lambda$ being the bench width coefficient. The slope is reinforced with a row of equally spaced piles is considered, as sketched in Fig. 1. The upper (lower) stage is denoted with an inclination angle $\beta_1$ ($\beta_2$) with a height of $\alpha_1 H$ ($\alpha_2 H$). $\alpha_1$ and $\alpha_2$ are depth coefficients that satisfy $\alpha_1 + \alpha_2 = 1.0$. The surcharge load and the seismic action are both involved in the context of kinematic limit analysis. The seismic excitation is considered based on a pseudo-static assumption and only the horizontal seismic excitation is considered in the analysis.

In the application of the kinematic limit theorem, a primary issue arises as to the construction of a 3D kinematically admissible velocity field. In this paper, the classical horn-shape curvilinear cone failure mechanism characterized with an apex angle of $2\phi'$ ($\phi'$ is soil friction angle) is employed, as schemed in Fig. 1. In the graph, the curvilinear cone intersects the stepped slope and passes through the slope toe and upper horizontal ground surface.

The upper and lower contours of the curvilinear cone on the neutral plane are two log-spirals, respectively. The cross-sections of the cone are all right circles defined by radius $R$, which is a function with respect to the rotation angle $\theta$. Conventionally, a stepped slope with the upper

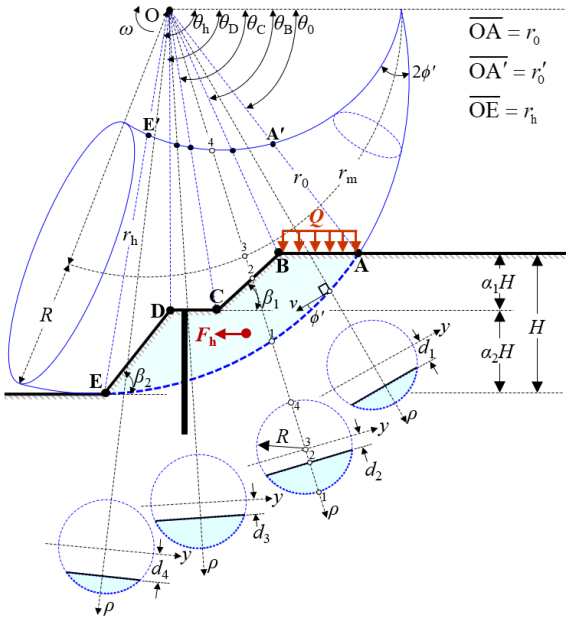


Fig. 1 3D rotational failure mechanism for a pile stabilized stepped slope

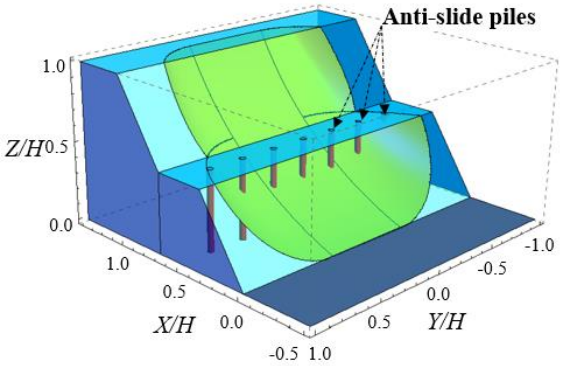


Fig. 2 Slip surface for a stepped slope stabilized by a row of anti-slide piles

inclination angle $\beta_1$ greater than the lower inclination $\beta_2$ ($\beta_1 > \beta_2$) is named a concave slope, and vice versa (Sun *et al*. 2017). More specially, a single stage slope is yield when $\beta_1 = \beta_2$ and the bench width becomes zero.

In 3D kinematic limit methods, this mechanism is routinely adjusted to incorporate a plane strain block to account for the 3D effects (e.g., Zheng *et al*. 2020, Park *et al*. 2021), as elucidated in Fig. 2. The 2D portion is a straightforward extension of the log-spiral failure mechanism (Chen 1975), while the 3D portion resembles with the 3D horn-shape failure mechanism partially. The relation between the width of the plane block and the total width of the sliding soil mass bears sole function relation, and can be determined easily according to the geometric relationship.

### 2.2 Reinforcement of stabilizing piles

For stepped earth slopes, the stabilizing piles locate in the slope with a horizontal distance $L_x$ (i.e., the pile location, see Fig. 3) measured from the slope toe. By

normalizing the pile location $L_x$ to the distance $L$, i.e., $L_x/L$ with $L$ being the projection of slope surface on the horizontal plane, the impact of pile location on the pile reinforcement can be described more conveniently. $L$ can be easily found from the geometrical relationship as

$$L=\frac{\alpha_1 H}{\tan\beta_1}+\lambda H+\frac{\alpha_2 H}{\tan\beta_2} \tag{1}$$

The piles move from the slope toe to the slope shoulder as $L_x/L$ increases from 0 to 1. The piles are driven to a design depth that beneath the slip surface and the intersection with slip surface is denoted by point P. In a polar system, the coordinates of point P can be found as $r_p$ and $\theta_p$, as illustrated in Fig. 4. In the analysis, the pile location is predetermined, and the relation between $L_x$ and $\theta_p$ can be solved from the following equation

$$\begin{aligned} L_x = {} & r_0\exp\left[(\theta_p-\theta_0)\tan\phi'\right]\cos\theta_p \\ & -r_0\exp\left[(\theta_h-\theta_0)\tan\phi'\right]\cos\theta_h \end{aligned} \tag{2}$$

The distribution of soil resistance acting on anti-slide piles is critical in stability analyses of piled slopes and should be estimated as accurate as possible. Robust numerical techniques and numerous model tests are routinely adopted to estimate the internal force (e.g., Hajiazizi and Heydari 2019, Zhong *et al*. 2019, Ersoy *et al*. 2020, Gonzalez *et al*. 2020, Liu *et al*. 2020, Sobhey *et al*. 2021). These numerical techniques possess great advantages in modeling the true field conditions, but high cost and specific skills are usually demand in performing these numerical simulations.

For analytical techniques, theoretical solutions with respect to the lateral force distribution models are not common. With this regard, Ito and Matsui (1975) established a theory to predict the lateral force acting on anti-slide piles based on plastic deformation assumptions. Applicability of the theory was formerly examined in the design of pile reinforced slopes. The soil behaves as a Mohr-Coulomb material and the soil around piles is postulated to be in a limit plastic state and an arching zone takes place. The lateral force acting on the stabilizing piles can be expressed analytically as

$$\begin{aligned} p(z) = {} & c'D_c\left(\frac{D_c}{D_n}\right)^A\left[\frac{1}{N_{\phi'}\tan\phi'}(C-2N_{\phi'}^{1/2}\tan\phi'-1)+\frac{B}{A}\right] \\ & -c'\left(D_c\frac{B}{A}-2D_nN_{\phi'}^{-1/2}\right)+\frac{\gamma z}{N_{\phi'}}\left[D_c\left(\frac{D_c}{D_n}\right)^A C-D_n\right] \end{aligned} \tag{3}$$

where $D_c$ and $D_n$ are center-to-center spacing and net intervals between neighboring piles, as sketched in Fig. 3; $\gamma$ is soil unit weight; and $z$ is a depth measured from the ground surface. It should be underlined that $D_n$ should not be too large to make this equation valid (Ito and Matsui 1975). The expressions of variables $N_{\phi'}$, $A$, $B$ and $C$ in Eq. (3) take the following form as

$$N_{\phi'}=\tan^2\left(\frac{\pi}{4}+\frac{\phi'}{2}\right) \tag{4a}$$

$$A=N_{\phi'}^{1/2}\tan\phi'+N_{\phi'}-1 \tag{4b}$$

$$B=2\tan\phi'+2N_{\phi'}^{1/2}+N_{\phi'}^{-1/2} \tag{4c}$$

$$C=\exp\left[\frac{d_p}{D_n}N_{\phi'}\tan\phi'\tan\left(\frac{\pi}{8}+\frac{\phi'}{4}\right)\right] \tag{4d}$$

where $d_p$ is the pile diameter (i.e., $d_p = D_c - D_n$).

## 3. Energy balance equation formulation

A balance equation of work rates is formulated by equaling the work rates of external loads to the energy dissipation rate according to the virtual work principle. In present analysis, the external forces include the soil gravity, surcharge loads and the seismic action, while the energy is dissipated because of soil cohesion and the resistances force of stabilizing piles. The balance equation of work rates is written as

$$W_\gamma+W_Q+W_s=D_{c'}+D_p \tag{5}$$

where $W_\gamma$, $W_Q$, $W_s$ are the work rates done by the soil gravity, the surcharge load and the seismic force; $D_{c'}$ and $D_p$ are the work dissipation rate of soil cohesion and pile resistance forces.

### 3.1 Work rates of soil gravity

The whole failure mechanism consists of the 3D curvilinear cone mechanism and the central 2D plane insert. Consequently, the work rate done by soil gravity can be computed separately as

$$W_\gamma=W_\gamma^{3D}+W_\gamma^{insert} \tag{6}$$

For the 3D curvilinear cone, a local coordinate system is introduced to calculate the work rate of soil gravity, which can be written as

$$W_\gamma^{3D}=\gamma\int_V v\cos\theta dV \tag{7}$$

where $v$ is the velocity corresponding to the infinitesimal volume element $dV$. For stepped slopes, the work rate of soil gravity can be expressed in terms of multiple integrations as

$$\begin{aligned} W_\gamma^{3D} = {} & 2\omega\gamma\left\{\int_{\theta_0}^{\theta_B}\int_0^{\sqrt{R^2-d_1^2}}\int_{d_1}^{\sqrt{R^2-x^2}}(r_m+y)^2\cos\theta dydxd\theta\right. \\ & +\int_{\theta_B}^{\theta_C}\int_0^{\sqrt{R^2-d_2^2}}\int_{d_2}^{\sqrt{R^2-x^2}}(r_m+y)^2\cos\theta dydxd\theta \\ & +\int_{\theta_C}^{\theta_D}\int_0^{\sqrt{R^2-d_3^2}}\int_{d_3}^{\sqrt{R^2-x^2}}(r_m+y)^2\cos\theta dydxd\theta \\ & \left.+\int_{\theta_D}^{\theta_h}\int_0^{\sqrt{R^2-d_4^2}}\int_{d_4}^{\sqrt{R^2-x^2}}(r_m+y)^2\cos\theta dydxd\theta\right\} \end{aligned} \tag{8}$$

where $\omega$ is angular velocity; $r_m$ represents the centerline of the conical volume; parameters $d_1$, $d_2$, $d_3$, $d_4$ and angles $\theta_0$, $\theta_B$, $\theta_C$, $\theta_D$, $\theta_h$ are depicted in Fig. 1 and can be found in Appendix.

The work rate of soil gravity of the insert can be easily computed by multiplying the results under a 2D situation by its width. It should be highlighted that, the methodology pioneered originally by Chen (1975) was routinely used to calculate the work rate under 2D conditions. Whereas for slopes with complicated configurations, this method might be overelaborated. On this regard, the method based on the volume integration of rotation bodies proposed by the authors (Wang *et al*. 2019) takes some advantages. For the plane insert, the work rate done by soil gravity can be written as

$$W_\gamma^{\text{insert}} = 0.25b\gamma r_0^3 \omega f_1 \tag{9}$$

Here, $b$ is the insert width and $f_1$ is a parameter relates to the failure mechanism geometry and can be found in Appendix.

### 3.2 Work rates of surcharge load

The work rate done by surcharge $Q$ can be calculated separately as

$$\begin{aligned} W_Q &= bL_{AB}Q\omega\left(r_0\cos\theta_0 - 0.5L_{AB}\right) \\ &+2Q\omega r_0^2\sin^2\theta_0\int_{\theta_0}^{\theta_B}\frac{\cos\theta}{\sin^3\theta}\sqrt{R^2-d_1^2}\,d\theta \end{aligned} \tag{10}$$

Here, the two terms on the right-hand denote the work rate of surcharge load corresponding to the plane insert and the curvilinear cone mechanism, respectively. $L_{AB}$ represents the horizontal distance between point $A$ and point $B$, as shown in Fig. 3 and is reported in Appendix.

### 3.3 Work rates of seismic force

From the perspective of limit analysis, the seismic excitation is commonly considered based on the pseudo-static assumptions. Though approximate, this approach bears an advantage in accumulating experience and therefore is widely used in the seismic stability evaluations of geotechnical structures (He *et al.* 2015, Wang *et al.* 2021).

By treating the seismic excitation as a uniformly distributed inertial force applying at the center of the sliding soil mass, the work rates of seismic loads can be calculated separately as

$$\begin{aligned} W_s^{3D} = 2\omega\gamma k_{hE}\Bigg\{ &\int_{\theta_0}^{\theta_B}\int_0^{\sqrt{R^2-d_1^2}}\int_{d_1}^{\sqrt{R^2-x^2}}(r_m+y)^2\sin\theta\,dy\,dx\,d\theta \\ &+\int_{\theta_B}^{\theta_C}\int_0^{\sqrt{R^2-d_2^2}}\int_{d_2}^{\sqrt{R^2-x^2}}(r_m+y)^2\sin\theta\,dy\,dx\,d\theta \\ &+\int_{\theta_C}^{\theta_D}\int_0^{\sqrt{R^2-d_3^2}}\int_{d_3}^{\sqrt{R^2-x^2}}(r_m+y)^2\sin\theta\,dy\,dx\,d\theta \\ &+\int_{\theta_D}^{\theta_h}\int_0^{\sqrt{R^2-d_4^2}}\int_{d_4}^{\sqrt{R^2-x^2}}(r_m+y)^2\sin\theta\,dy\,dx\,d\theta\Bigg\} \end{aligned} \tag{11}$$

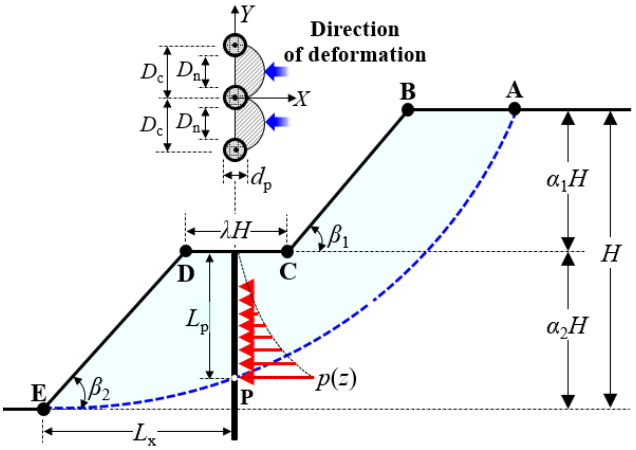


Fig. 3 Schematic diagram of forces and pile distribution

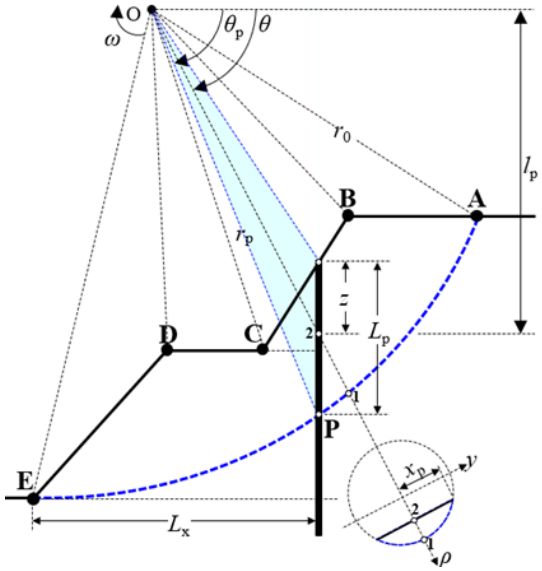


Fig. 4 Notions and conventions for calculation of the work dissipation rate due to the resistance of piles

and

$$W_s^{\text{insert}} = 0.25b\gamma r_0^3\omega k_{hE} f_2 \tag{12}$$

where $k_{hE}$ is the horizontal seismic coefficient and the parameter $f_2$ can be found in Appendix.

### 3.4 Wok rate dissipation of soil cohesion

For the 3D curvilinear cone failure mechanism, the total energy dissipation rate involves that of the deforming volume and that of the slip surface, i.e.

$$D_{c'}^{3D} = c'\cot\phi'\int_{S_{rem}} v_i n_i dS_{rem} \tag{13}$$

In Eq. (13), variable $S_{rem}$ denotes the surface exposed to air. For the stepped slopes in this study, $S_{rem}$ equals to the summation of surface $S_{AB}$, $S_{BC}$, $S_{CD}$, and $S_{DE}$. Therefore, the energy dissipation rate of soil cohesion takes the following form as

$$D_{c'}^{3D} = c'\cot\phi'\left\{\int_{S_{AB}} v_i n_i dS_{AB} + \int_{S_{BC}} v_i n_i dS_{BC} + \int_{S_{CD}} v_i n_i dS_{CD} + \int_{S_{DE}} v_i n_i dS_{DE}\right\} = -2\omega c'\cot\phi' r_0^3 f_3 \quad (14)$$

where parameter $f_3$ can also be found in Appendix.

For the plane strain insert, the energy dissipation rate occurs along the slip surface merely and can be computed by integrating the dot product of velocity and soil cohesion along the whole slip surface as

$$D_{c'}^{\text{insert}} = \omega b c' r_0^2 \int_{\theta_0}^{\theta_h} \exp\left[2(\theta-\theta_0)\tan\phi'\right] d\theta \quad (15)$$

### 3.5 Wok rate dissipation of pile reinforcement

The work dissipation rate of pile lateral resistance per unit thickness of soil layer equals to the product of the lateral force and the corresponding velocity, i.e.

$$dD_p = \omega p(z) l_p dz \quad (16)$$

where $l_p$ denotes the arm of the lateral force. The height of anti-slide piles above the slip surface $L_p$ can be found from the geometrical and trigonometric relation as

$$L_p = L_x\tan\beta_2 + r_0\exp\left[(\theta_p-\theta_0)\tan\phi'\right]\sin\theta_p - r_0\exp\left[(\theta_h-\theta_0)\tan\phi'\right]\sin\theta_h \quad (0 \le L_x \le \alpha_2 H\cot\beta_2) \quad (17a)$$

$$L_p = \alpha_2 H + r_0\exp\left[(\theta_p-\theta_0)\tan\phi'\right]\sin\theta_p - r_0\exp\left[(\theta_h-\theta_0)\tan\phi'\right]\sin\theta_h \quad (\alpha_2 H\cot\beta_2 \le L_x \le \alpha_2 H\cot\beta_2 + \lambda H) \quad (17b)$$

$$L_p = \alpha_2 H + (L_x - \alpha_2 H\cot\beta_2 - \lambda H)\tan\beta_1 + r_0\exp\left[(\theta_p-\theta_0)\tan\phi'\right]\sin\theta_p - r_0\exp\left[(\theta_h-\theta_0)\tan\phi'\right]\sin\theta_h \quad (\alpha_2 H\cot\beta_2 + \lambda H \le L_x \le \alpha_2 H\cot\beta_2 + \lambda H + \alpha_1 H\cot\beta_1) \quad (17c)$$

Similarly, the energy dissipation rate of pile resistance involves the energy dissipated within the two ends of the 3D composited mechanism and that dissipated within the central cylindrical plane strain insert, which can be derived as follows

$$D_p^{3D} = 2\omega r_0 \int_0^{L_p} l_p x_p \frac{p(z)}{D_c}\frac{\exp\left[(\theta_p-\theta_0)\tan\phi'\right]\cos\theta_p}{\cos^2\theta} dz \quad (18)$$

$$D_p^{2D} = 2\omega r_0 b \int_0^{L_p} l_p \frac{p(z)}{D_c}\frac{\exp\left[(\theta_p-\theta_0)\tan\phi'\right]\cos\theta_p}{\cos^2\theta} dz \quad (19)$$

where parameters $\theta$, $x_p$ and $l_p$ are denoted in Fig. 4 and can be expressed as

$$\theta = \arccos\left\{\frac{r_0\exp\left[(\theta_p-\theta_0)\tan\phi'\right]\cos\theta_p}{\sqrt{\left(r_0\exp\left[(\theta_p-\theta_0)\tan\phi'\right]\cos\theta_p\right)^2 + l_p^2}}\right\} \quad (20)$$

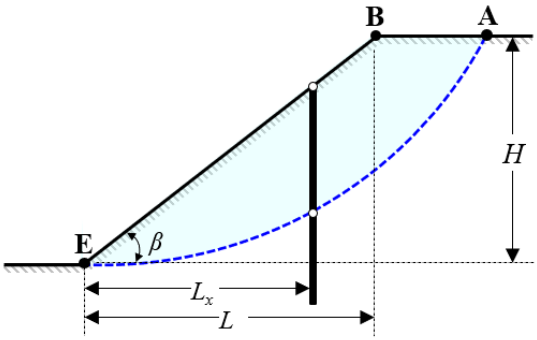


| Slope A | Slope B | Slope C |
|---|---|---|
| $\alpha_1 = 0.5$ | $\alpha_1 = 0.5$ | $\alpha_1 = 0.5$ |
| $\beta = \beta_1 = \beta_2 = 45^\circ$ | $\beta = \beta_1 = \beta_2 = 35^\circ$ | $\beta = \beta_1 = \beta_2 = 45^\circ$ |
| $\lambda = 0$ | $\lambda = 0$ | $\lambda = 0$ |
| $H = 20$ m | $H = 12$ m | $H = 10$ m |
| $c' = 38$ kPa | $c' = 24$ kPa | $c' = 23.94$ kPa |
| $\phi' = 20^\circ$ | $\gamma = 18$ kN/m$^3$ | $\phi' = 10^\circ$ |
| $\gamma = 19$ kN/m$^3$ | $Q = 0$ | $\gamma = 19.63$ kN/m$^3$ |
| $Q = 0$ | $D_c = 4.0$ m | $Q = 0$ |
| $k_{hE} = 0$ | $D_n = 3.4$ m | $k_{hE} = 0$ |
| | $d_p = 0.6$ m | $D_c = 1.5$ m |
| | $L_x = 8.6$ m | $D_n = 1.2$ m |
| | | $D_c/d_p = 5.0$ |

Fig. 5 Parameters for soil property, slope configuration and pile reinforcement for the illustrative slope

$$x_p = \sqrt{R^2 - \left[\sqrt{l_p^2 + (r_p\cos\theta_p)^2} - r_m\right]^2} \quad (21)$$

$$l_p = r_0\exp\left[(\theta_p-\theta_0)\tan\phi'\right]\sin\theta_p - L_p + z \quad (22)$$

The gravity increase technique was employed to define the factor of safety (FOS) of stepped earth slopes, which can be written as a ratio between the total internal energy dissipation rate and the total external work rate as

$$\text{FOS} = \frac{D_{c'} + D_p}{W_\gamma + W_Q + W_s} \quad (23)$$

An optimization procedure was developed based on the *MATHEMATICA* software to search for the global minimum FOS. In the searching progress, some geometrical constraints should be meet, i.e., $|d_1| < R$, $|d_2| < R$, $|d_3| < R$, $|d_4| < R$, $0 < r_0'/r_0 < 1.0$, $0 < \theta_0 < \theta_B < \theta_C < \theta_D < \theta_h < \pi$.

### 3.6 Verification

Comparisons with published 2D and 3D solutions were performed to verify the effectiveness of the proposed method. An illustrative slope was reexamined and the parameters for soil properties, slope configurations and pile reinforcements are denoted in Fig. 5. For Slope A without piles, the FOSs presented by Rao *et al*. (2020) and by this paper are summarized in Table 1. Evidently, the results in this paper are consistent with the published ones, indicating the effectiveness of the proposed method in the stability assessments of slopes without piles.

Table 1 Comparisons of FOSs for Slope A without piles

| *B/H* | 2 | 5 | 10 | 2D |
|---|---|---|---|---|
| Rao *et al*. (2020) | 1.956 | 1.741 | 1.677 | 1.618 |
| Present study | 1.984 | 1.758 | 1.685 | 1.629 |

Table 2 Comparisons of the critical acceleration coefficient $k_c$ for Slope B

| | | *B/H*=2 | | *B/H*=5 | | *B/H*=10 | |
|---|---|---|---|---|---|---|---|
| | | $\phi'$=10° | $\phi'$=15° | $\phi'$=10° | $\phi'$=15° | $\phi'$=10° | $\phi'$=15° |
| Without piles | Present study | 0.203 | 0.309 | 0.129 | 0.231 | 0.109 | 0.211 |
| | He *et al*. (2015) | 0.199 | 0.307 | 0.125 | 0.228 | 0.105 | 0.208 |
| With piles | Present study | 0.251 | 0.358 | 0.178 | 0.280 | 0.158 | 0.258 |
| | He *et al*. (2015) | 0.244 | – | 0.184 | 0.275 | 0.159 | 0.252 |

Table 3 Comparisons of FOSs for Slope C with piles

| $L_x/L$ | 0.0 | 0.2 | 0.4 | 0.6 | 0.8 | 1.0 |
|---|---|---|---|---|---|---|
| Gao *et al*. (2015) | 1.275 | 1.397 | 1.576 | 1.761 | 1.835 | 1.602 |
| Present study | 1.286 | 1.393 | 1.559 | 1.745 | 1.851 | 1.625 |

In addition, to check the applicability of the proposed method in seismic slope stability estimations, a further comparison was carried out between the critical acceleration coefficients (i.e., the seismic coefficient that brings the slope in a limit equilibrium state) for Slope B provided by He *et al*. (2015) and this paper. The cases with and without piles are both considered and the results are listed in Table 2. As shown in the table, the results obtained by these two methods also exhibit good agreement.

For piled Slope C with different pile locations, the FOSs provided by Gao *et al*. (2015) and by this paper are also presented in Table 3 for comparisons. Clearly, the results exhibit good agreement with each other. Therefore, the comparisons in Tables 1-3 demonstrate good performance of the proposed method in piled slope stability estimations. In the following analyses, the illustrative Slope C is still utilized to investigate the reinforcement of stabilizing piles on the stability of 3D stepped slopes. The parameters correspond to $H$ = 10 m, $B/H$ = 2, $\alpha$ = 0.5, $\lambda$ = 0.2, $\beta_1$ = 60°, $\beta_2$ = 45°, $\phi'$ = 10°, $c'$ = 23.94 kPa, $\gamma$ = 19.63 kN/m$^3$, $D_c$ = 1.5 m, $D_n$ = 1.2 m, $Q$ = 0 and $k_{hE}$ = 0.

## 4. Results

To quantitatively describe the pile reinforcement on the safety of stepped earth slopes, the percentage of the increase in FOS of stepped slopes due to the presence of piles FOSI (%) was introduced and can be assessed using the following formula, i.e.

$$\mathrm{FOSI} = \frac{\mathrm{FOS}_{\text{with piles}} - \mathrm{FOS}_{\text{without piles}}}{\mathrm{FOS}_{\text{without pilesss}}} \times 100\% \tag{24}$$

where $\mathrm{FOS}_{\text{with piles}}$ denotes the FOS of stabilized stepped slopes and $\mathrm{FOS}_{\text{without piles}}$ denotes the FOS of slopes without piles.

### 4.1 Effect of pile location

Fig. 6 elucidates the influence of pile location on the stability of pile stabilized stepped slopes. In the calculation, the pile location is altered from the slope toe to the slope shoulder. The impacts of bench width coefficient $\lambda$, depth coefficient $\alpha_1$, internal frictional angle $\phi'$, slope height $H$, lower inclination angle $\beta_2$, upper inclination angle $\beta_1$, horizontal seismic coefficient $k_{hE}$ and surcharge load $Q$ on pile reinforcements are investigated in sequence.

Notably, the pile reinforcement in stepped earth slopes differ significantly with that in single stage slopes (Wang *et al*. 2020). The optimum pile location depends closely on soil properties and slope configurations. Generally, the pile reinforcement increases evidently when the piles are moved from the slope toe to the shoulder of the lower stage, then decreases slightly when the piles continually move to the toe of the upper stage, and finally increases as the piles move on and an optimum pile location exists for most cases. It can be summarized that, the curves that the pile reinforcement varies with pile location can be divided into three sections, i.e., “the lower growth section”, “the middle decrease section”, and “the upper continued growth section”. This means that, when the piles are installed in the bench, they should be inserted as close to the bench shoulder as possible at the convenience of construction.

For stepped slopes, the slope stability and the pile reinforcement relate significantly to the bench width, as shown in Fig. 6(a). The optimum pile location lies abound $L_x/L$ = 0.9 universally. For $L_x/L$ = 0.5, FOSs are 1.170, 1.204, 1.241, 1.279, 1.320 and 1.361 corresponding to $\lambda$ = 0, 0.05, 0.10, 0.15, 0.20 and 0.25. The slope becomes more stable as the bench width increases, while the pile reinforcement varies dramatically as shown in the graph.

When the piles are installed in the upper stage of the slope, the pile reinforcement decreases as the bench width increases. When they are inserted in the lower stage,

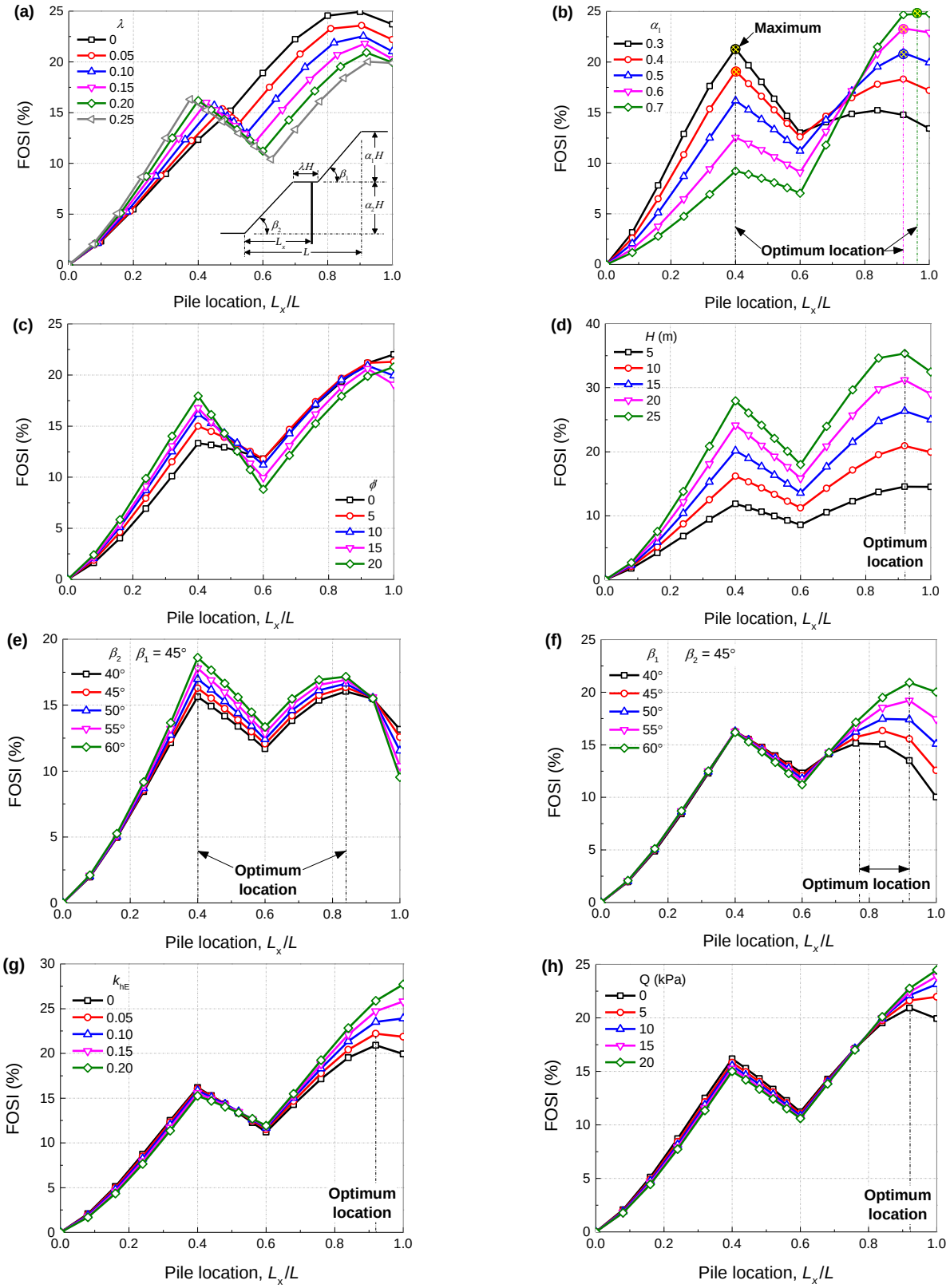


Fig. 6 Effect of pile location on the stability of pile stabilized stepped slopes with different values of: (a) step width $\lambda$, (b) depth coefficient $\alpha$, (c) internal frictional angle $\phi'$, (d) slope height $H$, (e) slope angle $\beta_2$, (f) slope angle $\beta_1$, (g) horizontal seismic coefficient $k_{hE}$ and (h) surcharge load $Q$

however, the pile reinforcement increases as the bench width increases.

The depth coefficient is critical for the optimum pile location determination, as shown in Fig. 6(b). The optimum pile location is $L_x/L = 0.4$ when $\alpha_1 \leq 0.4$, but is around $L_x/L$ with smaller depth coefficients, the optimum pile location

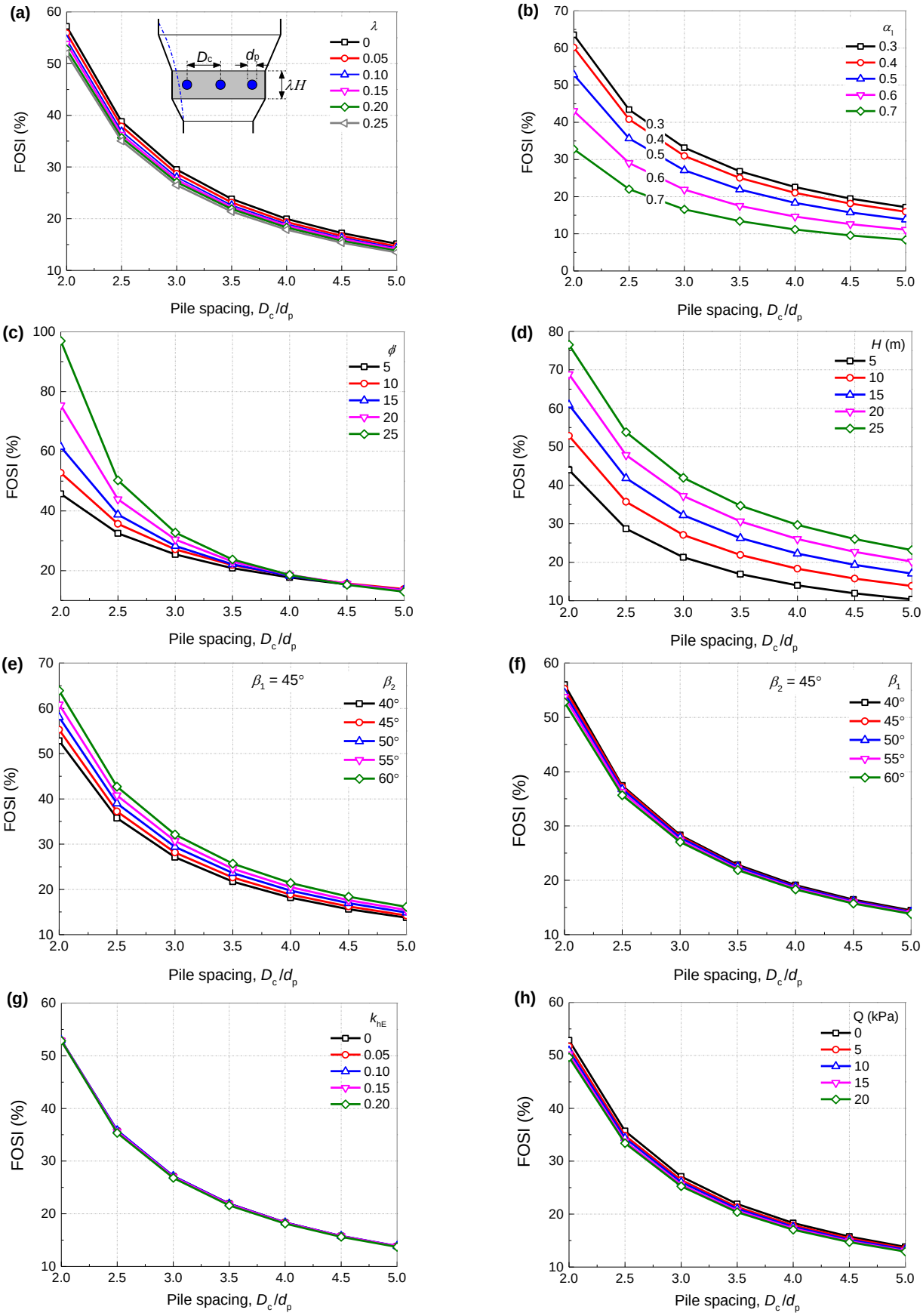


Fig. 7 Effect of pile spacing on the stability of pile stabilized stepped slopes with different values of: (a) step width $\lambda$, (b) depth coefficient $\alpha$, (c) internal frictional angle $\phi'$, (d) slope height $H$, (e) slope angle $\beta_2$, (f) slope angle $\beta_1$, (g) horizontal seismic coefficient $k_{hE}$ and (h) surcharge load $Q$

= 0.94 when $\alpha_1 \geq 0.5$. This implies that, for stepped slopes on lies in the lower portion of the slope, and vice versa.

The internal friction angle influences the optimum pile location slightly, as shown in Fig. 6(c). The optimum location lies around $L_x/L = 0.92$ when $\phi'$ falls in 10° ~ 15°, and vanishes when $\phi'$ is beyond this range. However, for stepped slopes with larger $\phi'$ values, the pile reinforcement increases when the piles are installed in the lower part of the slope, and vice versa.

The slope height imposes no influence on the optimum pile location, as shown in Fig. 6(d). For slopes with different heights, the optimum location all lies around $L_x/L = 0.92$. But the peak becomes more obvious and the pile reinforcement increases significantly as the slope height increases. For example, for stepped slopes with the pile location $L_x/L = 0.4$, the pile reinforcement is 11.8%, 20.2% and 27.9% corresponding to $H = 5$ m, 15 m and 25 m.

The slope inclination angle possesses different influence on the stability of pile reinforced stepped slopes, as illustrated in Figs. 6(e) and 6(f). The angle $\beta_2$ is more critical for the pile reinforcement and the optimum pile location. As illustrated in Fig. 6(e), for steep stepped slopes, the pile reinforcement is more significant and the optimum location lies around $L_x/L = 0.4$. For gentle slopes, however, the pile reinforcement is relatively indistinctive with the optimum pile location changing to $L_x/L = 0.83$. When angle $\beta_2$ is fixed and only angle $\beta_1$ is altered, as shown in Fig. 6(f), the pile reinforcement remains nearly unchanged when the piles are inserted in the lower portion of the slope. When the piles are installed in the upper portion of the slope, the pile reinforcement as well as the optimum pile location increases significantly as the upper inclination angle increases. The optimum pile location increases from $L_x/L = 0.77$ to $L_x/L = 0.93$, when $\beta_1$ increases from 40° to 60°.

The seismic excitation and surcharge load possess similar influence on the pile reinforcement and the optimum pile location, as demonstrated in Figs. 6(g) and 6(h). For piled stabilized stepped slopes subjected to strong earthquakes or heavy surcharge loads, the pile reinforcement is relatively insignificant when the piles are located in the lower portion of the slope, but is relatively prominent when the piles are inserted in the upper portion of the slope. In addition, the optimum pile location generally arounds $L_x/L = 0.93$ and vanishes gradually as the seismic excitation or the surcharge load increases.

### 4.2 Effect of pile spacing

Fig. 7 illustrates the influence of pile spacing on the stability of pile stabilized stepped slopes. In the analyses, the piles are located in the middle of the bench (i.e., $L_x/L = 0.50$) and only the pile spacing is altered. The aforementioned influence factors are also investigated in section. As expected, the pile reinforcement depends strongly on the pile group density (characterized by the pile spacing $D_c/d_p$) and declines conspicuously as the pile spacing increases.

Increasing the bench width has limited effect on the pile reinforcement, as shown in Fig. 7(a). The pile reinforcement is improved by a few percentage points for wider benches. When the pile spacing increase to $D_c/d_p = 5.0$, the pile reinforcement for stepped slopes with different bench widths declines to 15% universally.

The depth coefficient, however, influences the pile reinforcement significantly, as illustrated in Fig. 7(b). The pile reinforcement is pronounced in slopes with smaller depth coefficients, but is relatively less evident in slopes with lager depth coefficients. This phenomenon is more evident in slopes with denser pile group, but becomes less obvious in slopes with looser pile group. For example, for the pile spacing $D_c/d_p = 2.0$, FOSI = 63.5% and 32.7% corresponding to $\alpha_1 = 0.3$ and 0.7, respectively. The difference is 30.8% and reduces to 8.8% when the pile spacing is increased to $D_c/d_p = 5.0$.

The internal frictional angle affects the pile reinforcement remarkably, especially for slopes with denser pile group, as shown in Fig. 7(c). When the pile spacing $D_c/d_p \geq 4.0$, the pile reinforcement is insensitive to the internal frictional angle. In another word, in the design of stepped earth slopes, when the pile spacing $D_c/d_p \geq 4.0$, the impact of $\phi'$ on the pile reinforcement can be neglected. Conversely, for stepped slopes, no matter the pile group is dense or loose, the slope height possesses great impact on the pile reinforcement, as shown in Fig. 7(d). Similar to the influence of $\alpha_1$, the effect of slope height is evident for denser pile group, but is relatively less evident for loose pile group.

The upper and lower inclination angles, the seismic excitation and the surcharge load possess little influence on the pile reinforcement, as depicted in Figs. 7(e)-(7h). The pile reinforcement increases as $\beta_2$ increases, increases slightly as $\beta_1$ and $Q$ decreases, but remains nearly unchanged as the seismic load increases.

### 4.3 3D effect

Fig. 8 illustrates the relationship between the 3D effect and the safety of pile stabilized stepped slopes considering the seismic excitation and the surcharge load. As expected, the slope safety relates closely to its width, and is significantly reduced when subjected to seismic and surcharge loads. The 3D solutions decrease nonlinearly as the slope width increases, and finally approaches the 2D ones. The slope safety reduces nearly linearly as the seismic load increases, but presents nearly linear shapes as the surcharge load increases. Furthermore, as indicated in the graph, the 3D effect is insensitive to the seismic excitation, but becomes relatively sensitive to the surcharge load. The difference between FOSs corresponding to $B/H = 1$ and the 2D cases remains identical as the seismic load increases, but declines as surcharge load increases.

### 4.4 3D critical slip surface

Fig. 9 demonstrates the influence of pile installation on the 3D critical slip surface of stepped slopes. Fig. 9(a) depicts the slip surface on the symmetry plane and Fig. 9(b) presents the whole slip surface in a 3D version. The piles are installed in the middle of the bench. It can be observed

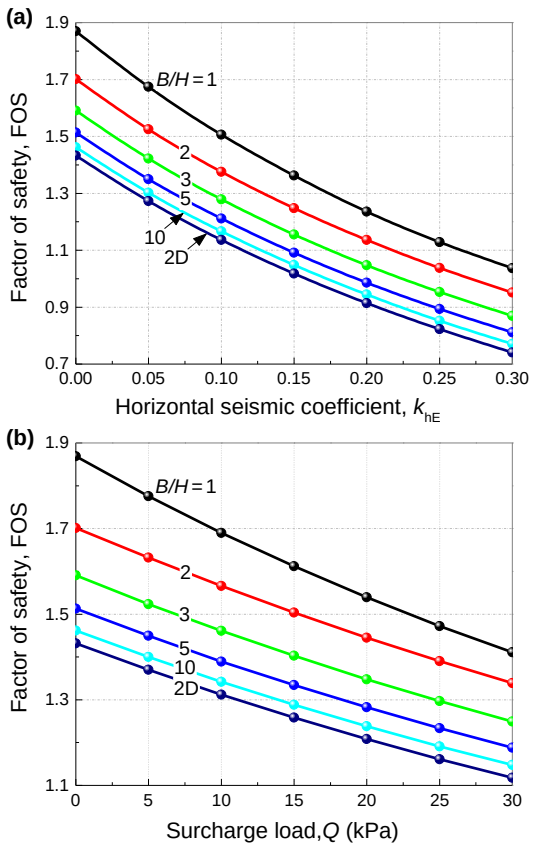


Fig. 8 Effect of (a) horizontal seismic coefficient $k_{hE}$ and (b) surcharge load $Q$ on the stability of pile stabilized slopes with different widths

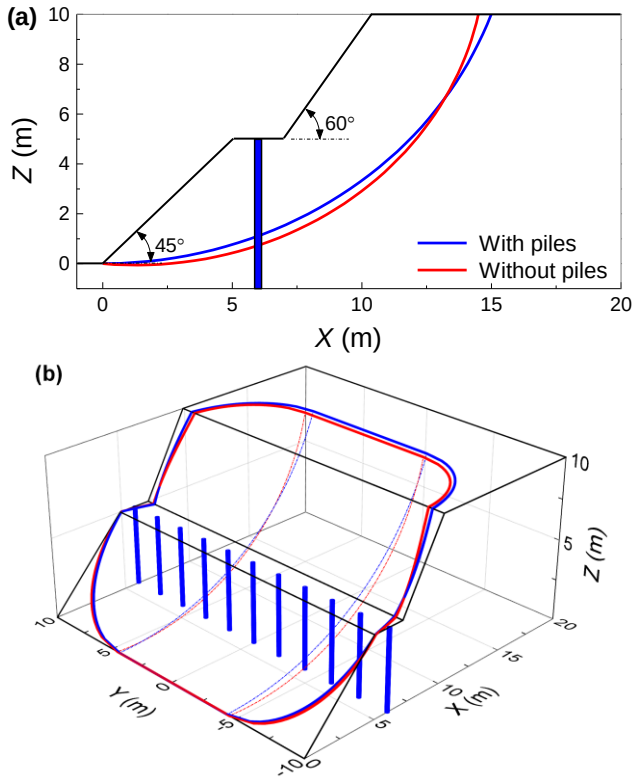


Fig. 9 Reinforcement of anti-slide piles on slope critical slip surface: (a) the symmetry plane view and (b) the 3D view

evidently that, compared with that for no pile slope, the slip surface becomes much shallower when the stabilizing piles are inserted in the middle of the bench. The slip surface on the slope crest, however, departs from the slope shoulder. In the 3D version of the slip surface, the slip surface in the width direction becomes wider compared with that of no pile slopes. The width of the plane insert becomes narrower when the piles are utilized to reinforce the slope.

## 5. Conclusions

This paper performed a kinematic limit analysis for the stability of 3D pile stabilized stepped slopes and considered the seismic and surcharge loads. The differences between 2D and 3D methods, the influences of slope shapes and pile design parameters on stepped slope stability, and the impacts of seismic and surcharge loads on piled slope stability are mainly investigated. A series of parametric studies were carried out to illustrate the pile location, pile density, 3D effects, surcharge load, seismic action and slope shape on the stability of pile stabilized stepped slopes. The findings are summarized as follows.

- The optimum pile location and the pile reinforcement in stepped slopes differ with that in single stage slopes significantly. The optimum pile location generally lies in the upper portion of the slope around $L_x/L$ = 0.9, or may lies in the shoulder of the bench (i.e., $L_x/L$ = 0.4 in this analysis). The pile reinforcement becomes less pronounced when the piles are installed in the upper portion of the slope. When the depth coefficient increases α1, the optimum pile location moves from the bench shoulder to the slope upper portion. In high stepped slopes, the pile reinforcement becomes more evident. When the lower stage of the slope is steep, the pile reinforcement is enhanced slightly, and the optimum pile location may lie in the bench shoulder. Conversely, when the upper stage is steep, the pile reinforcement is improved evidently only when the piles are located in the upper portion of the slope, and the optimum pile location moves towards to the slope shoulder. The seismic excitation and surcharge load have influence only when the piles are installed in the slope upper portion.
- The pile reinforcement is improved obviously as the pile density increases universally. The pile reinforcement reaches 10% universally for a pile spacing $D_c/d_p$ = 5.0, and approaches 70% (the specific value depends on soil parameters and slope configurations) when the pile spacing reaches $D_c/d_p$ = 2.0. The pile reinforcement is more sensitive to the depth coefficient when the pile group is denser, and vice versa. The influence of internal frication angle $\phi'$ on the pile reinforcement gets more pronounced when the pile spacing $D_c/d_p \leq 4.0$, and nearly vanishes when $D_c/d_p > 4.0$. The slope inclination angle, seismic excitation and surcharge load show limited influence on the pile reinforcement for stepped slopes with different pile densities.
- The seismic excitation and surcharge load have negative impacts on stability of pile stabilized slopes. The 3D solution decreases nonlinearly as the slope width increases, and finally approaches that of the 2D ones as the

slope width approaches $B/H$ = 10. The slope safety reduces nonlinearly as the seismic load increases, but nearly as the surcharge load increases. The 3D effect is insensitive to the seismic excitation, but is relatively sensitive to the surcharge load.

- Compared with that for no pile slope, the slip surface becomes much shallow when the anti-slides are installed in the middle of the bench. The slip surface on the slope crest departs from the slope shoulder, and the slip surface in the width direction becomes wider.

## Acknowledgments

This research was financially supported by the National Natural Science Foundation of China (Grant Nos. 52208345, 52168046, 41867034, 42272312), the Opening Fund of State Key Laboratory of Geohazard Prevention and Geoenvironment Protection (Grant No. SKLGP2022K002), the Natural Science Foundation of Jiangsu Province (Grant No. BK20210479) and the Systematic Project of Guangxi Key Laboratory of Disaster Prevention and Engineering Safety (Grant No. 2020ZDK010). The authors appreciate all the financial supports greatly.

## References

Chen, B., Gao. Y., Sun, D. and Li, J. (2021), "Simple testing method for measuring the triaxial stress-strain relations of unsaturated soils at high suctions", *Geotech. Test J.*, **44**(2), 20190278. https://doi.org/10.1520/GTJ20190278.

Chen, B., Peng, F., Zhang, L. and Sun, D. (2023), "Investigation on swelling characteristics of GMZ bentonite with different initial water contents", *Ann. Nucl. Energy*, **181**, 109565. https://doi.org/10.1016/j.anucene.2022.109565.

Chen, W.F. (1975). *Limit analysis and soil plasticity*. Amsterdam: Elsevier.

Deng, D.P., Li, L. and Zhao, L.H. (2017), "Limit-equilibrium method for reinforced slope stability and optimum design of antislide micropile parameters", *Int. J. Geomech.*, **17**(2), 06016019. https://doi.org/10.1061/(ASCE)GM.1943-5622.0000722.

Deng, D.P., Li, L. and Zhao, L.H. (2019), "Stability analysis of slopes under groundwater seepage and application of charts for optimization of drainage design", *Geomech. Eng.*, **17**(2), 181-194. http://dx.doi.org/10.12989/gae.2019.17.2.181.

Ersoy, H., Kaya, A., Angn, Z. and Dag, S. (2020), "2D and 3D numerical simulations of a reinforced landslide: A case study in NE Turkey", *J. Earth Syst. Sci.*, **129**(1), 82. https://doi.org/10.1007/s12040-020-1343-y.

Gao, Y.F., Ye, M. and Zhang, F. (2015), "Three-dimensional analysis of slopes reinforced with piles", *J. Centr. South U.*, **22**(6), 2322-2327. https://doi.org/10.1007/s11771-015-2757-6.

Gonzalez, Y.T., Schaefer, V.R. and Rollins, D.K. (2020), "Statistical assessment of factor of safety for pile-reinforced slopes", *J. Geotech. Geoenviron. Eng.*, **146**(9), 04020083. https://doi.org/10.1061/(ASCE)GT.1943-5606.0002323.

Hajiazizi, M. and Heydari, F. (2019), "Where is the optimal pile location on earth slopes?", *KSCE J. Civ. Eng.*, **23**(3), 1087-1094. https://doi.org/10.1007/s12205-019-1979-9.

He, Y., Hazarika H., Yasufuku, N., Han, Z. and Li, Y.G. (2015), "Three-dimensional limit analysis of seismic displacement of slope reinforced with piles", *Soil Dyn. Earthq. Eng.*, **77**, 446-452. https://doi.org/10.1016/j.soildyn.2015.06.015.

Hong, G.Q., Liu, W.H., Li, W.G., Hu, P., Huang, S.H. and Kong, G.Q. (2023), "Experimental investigation on expansion characteristics and strength of carbonating reactive magnesia solidified clay", *Case Stud. Constr. Mat.*, **18**, e01918. https://doi.org/10.1016/j.cscm.2023.e01918.

Ito, T. and Matsui, T. (1975), "Methods to estimate lateral force acting on stabilizing piles", *Soils Found.*, **15**(4), 43-59. https://doi.org/10.3208/sandf1972.15.4_43.

Lam, L. and Fredlund, D.G. (1993), "A general limit equilibrium model for three-dimensional slope stability analysis", *Can. Geotech. J.*, **30**(6), 905-919. https://doi.org/10.1139/t93-089.

Li, Q., Wang, Y.M., Zhang, K.B., Yu, H. and Tao, Z.Y. (2020), "Field investigation and numerical study of a siltstone slope instability induced by excavation and rainfall", *Landslides*, **17**(6), 1485-1499. https://doi.org/10.1007/s10346-020-01396-5.

Lim, K., Li, A.J., and Lyamin, A.V. (2015), "Three-dimensional slope stability assessment of two-layered undrained clay", *Comput. Geotech.*, **70**, 1-17. https://doi.org/10.1016/j.compgeo.2015.07.011.

Liu, D.Z., Hu, X.L., Zhou, C., Xu, C., He, C.C., Zhang, H. and Wang, Q. (2020), "Deformation mechanisms and evolution of a pile-reinforced landslide under long-term reservoir operation", *Eng. Geol.*, **275**, 105747. https://doi.org/10.1016/j.enggeo.2020.105747.

Liu, S.Y., Su, Z.N., Li, M. and Shao, L.T. (2020), "Slope stability analysis using elastic finite element stress fields", *Eng. Geol.*, **273**, 105673. https://doi.org/10.1016/j.enggeo.2020.105673.

Liu, Z.P., Liu, J., Bian, K. and Ai, F. (2019), "Three-dimensional limit equilibrium method based on a TIN sliding surface", *Eng. Geol.*, **262**, 105325. https://doi.org/10.1016/j.enggeo.2019.105325.

Michalowski, R.L. and Drescher, A. (2009), "Three-dimensional stability of slopes and excavations", *Géotechnique*, **59**(10), 839-850. https://doi.org/10.1680/geot.8.P.136.

Pan, Q.J., Chen, Z.Y., Wu, Y.M., Dias, D. and Oreste, P. (2021), "Probabilistic tunnel face stability analysis: A comparison between LEM and LAM", *Geomech. Eng.*, **24**(4), 399-406. https://doi.org/10.12989/gae.2021.24.4.399.

Pang, H.P., Nie, X.P., Sun, Z.B., Hou, C.Q., Dias, D. and Wei, B.X. (2020), "Upper bound analysis of 3D-reinforced slope stability subjected to pore-water pressure", *Int. J. Geomech.*, **20**(4), 06020002. https://doi.org/10.1061/(ASCE)GM.1943-5622.0001636.

Park, D. and Michalowski, R.L. (2021), "Three-dimensional stability assessment of slopes in intact rock governed by the Hoek-Brown failure criterion", *Int. J. Rock Mech. Min.*, **137**, 104522. https://doi.org/10.1016/j.ijrmms.2020.104522.

Rao, P.P., Wu, J. and Mo, Z.H. (2020), "3D limit analysis of the transient stability of slope during pile driving in nonhomogeneous and anisotropic soil", *Adv. Civ. Eng.*, **2020**(9), 1-10. https://doi.org/10.1155/2020/7560219.

Sobhey, M., Shahien, M., Sawwaf El, M. and Farouk, A. (2021), "Analysis of clay slopes with piles using 2D and 3D FEM", *Geotech. Geol. Eng.*, **39**, 2623-2631. https://doi.org/10.1007/s10706-020-01627-5.

Son, S.W., Im, J.C., Seo, M.S. and Hong, S.W. (2021), "Analysis of the correlation between the velocity speed of high-speed railways and the suppressing effect of lateral displacement of retaining wall according to the arrangement of stabilizing piles", *J. Korean Geosynth. Soc.*, **20**(1), 1-8. https://doi.org/10.12814/jkgss.2021.20.1.001.

Stark, T.D. and Eid, H.T. (1998), "Performance of three-dimensional slope stability methods in practice", *J. Geotech. Geoenviron. Eng.*, **124**(11), 1049-1060. https://doi.org/10.1061/(ASCE)1090-0241(1998)124:11(1049).

Sun, C.W., Chai, J.R., Xu, Z.G. and Qin, Y. (2017), "3D stability charts for convex and concave slopes in plan view with homogeneous soil based on the strength-reduction method", *Int. J. Geomech.*, **17**(5), 06016034. https://doi.org/10.1061/(ASCE)GM.1943-5622.0000809.

Wang, L., Hu, W., Gao, Y., Zhou, E.Q., Li, J., Chen, G.X, (2023) "Estimation of 3D earth pressure with inclined backfill surface considering seismic loads and suction effects", *Int. J. Numer. Anal. Met*., 1-14. http://doi.org/10.1002/nag.3499.

Wang, L., Hu. W., Sun, D.A. and Li, L. (2019), "3D stability of unsaturated soil slopes with tension cracks under steady infiltrations", *J. Numer. Anal. Met. Geomech.*, **43**(6), 1184-1206. https://doi.org/10.1002/ nag.2889.

Wang, L., Liu, W.H., Hu, W., Li, W.G. and Sun, D.A. (2021a), "Effects of seismic force and pore water pressure on stability of 3D unsaturated hillslopes", *Nat. Hazards*, **105**(2), 2093-2116. https://doi.org/10.1007/s11069-020-04391-0.

Wang, L., Sun D.A., Yao, Y.P., Wu, L.Z. and Xu, Y.F. (2020), "Kinematic limit analysis of three-dimensional unsaturated soil slopes reinforced with a row of piles", *Comput. Geotech.*, **120**: 103428. https://doi.org/10.1016/j.compgeo.2019.103428.

Wang, L., Xu, M.J., Li, J., Liu, W.H., and Sun, D.A. (2021b), "A new method for determination of 3D active earth pressure of unsaturated backfills", *KSCE J. Civ. Eng.*, **25**(12), 4631-4645. https://doi.org/10.1007/s12205-021-0508-9.

Zhao, L.H., Jiao, K.F., Zuo, S., Yu, C.H. and Tang, G.P. (2020), "Pseudo-static stability analysis of wedges based on the nonlinear barton-bandis failure criterion", *Geomech. Eng.*, **20**(4), 287-297. https://doi.org/10.12989/gae.2020.20.4.287.

Zheng, L., Li. L. and Li, J.P. (2020), "Development of three-dimensional failure mechanisms and genetic algorithm for limit analysis of two-layer slopes", *Nat. Hazards*, **103**(3), 3181-3212. https://doi.org/10.1007/s11069-020-04126-1.

Zhong, W., Yang, T., He, N. and Cosgrove, T. (2019), "Load-computational methods of anti-slide piles", *Cluster Comput.*, **22**, S8529-S8539. https://doi.org/10.1007/s10586-018-1893-9.

*CC*

## Appendix: Some equations

$$d_1 = r_0 \frac{\sin\theta_0}{\sin\theta} - r_{\mathrm{m}} \tag{1}$$

$$d_2 = r_0 \frac{\sin\theta_0 \sin(\theta_{\mathrm{B}} + \beta_1)}{\sin\theta_{\mathrm{B}} \sin(\theta + \beta_1)} - r_{\mathrm{m}} \tag{2}$$

$$d_3 = \frac{r_0 \sin\theta_0 + \alpha_1 H}{\sin\theta} - r_{\mathrm{m}} \tag{3}$$

$$d_4 = r_0 \exp\left[(\theta_{\mathrm{h}} - \theta_0)\tan\phi'\right] \frac{\sin(\theta_{\mathrm{h}} + \beta_2)}{\sin(\theta + \beta_2)} - r_{\mathrm{m}} \tag{4}$$

$$\begin{aligned} L_{\mathrm{AB}} = {} & r_0 \cos\theta_0 - r_0 \exp\left[(\theta_{\mathrm{h}} - \theta_0)\tan\phi'\right]\cos\theta_{\mathrm{h}} \\ & -(\alpha_1 \cot\beta_1 + \alpha_2 \cot\beta_2 + \lambda)H \end{aligned} \tag{5}$$

$$\theta_{\mathrm{B}} = \arctan\frac{r_0 \sin\theta_0}{r_0 \cos\theta_0 - L_{\mathrm{AB}}} \tag{6}$$

$$\theta_{\mathrm{C}} = \arctan\frac{r_0 \sin\theta_0 + \alpha_1 H}{r_0 \cos\theta_0 - L_{\mathrm{AB}} - \alpha_1 H \cot\beta_1} \tag{7}$$

$$\theta_{\mathrm{D}} = \arctan\frac{r_0 \exp\left[(\theta_{\mathrm{h}} - \theta_0)\tan\phi'\right]\sin\theta_{\mathrm{h}} - \alpha_2 H}{r_0 \exp\left[(\theta_{\mathrm{h}} - \theta_0)\tan\phi'\right]\cos\theta_{\mathrm{h}} + \alpha_2 H \cot\beta_2} \tag{8}$$

$$\begin{aligned} f_1 = {} & \int_{\theta_0}^{\theta_{\mathrm{B}}} \frac{\cos\theta}{\sin^3\theta} (\exp\left[(\theta - \theta_0)\tan\phi'\right]\sin\theta + \sin\theta_0)^2 \times (\exp\left[(\theta - \theta_0)\tan\phi'\right]\sin\theta - \sin\theta_0) d\theta \\ & + \int_{\theta_{\mathrm{B}}}^{\theta_{\mathrm{C}}} \frac{\cos\theta}{\sin^3\theta_{\mathrm{B}} \sin^3(\theta + \beta_1)} \left\{\exp\left[(\theta - \theta_0)\tan\phi'\right]\sin\theta_{\mathrm{B}} \sin(\theta + \beta_1) + \sin\theta_0 \sin(\theta_{\mathrm{B}} + \beta_1)\right\}^2 \\ & \times \left[\exp\left[(\theta - \theta_0)\tan\phi'\right]\sin\theta_{\mathrm{B}} \sin(\theta + \beta_1) - \sin\theta_0 \sin(\theta_{\mathrm{B}} + \beta_1)\right] d\theta \\ & + \int_{\theta_{\mathrm{C}}}^{\theta_{\mathrm{D}}} \frac{\cos\theta}{\sin^3\theta} \left\{\exp\left[(\theta - \theta_0)\tan\phi'\right]\sin\theta + \left[\sin\theta_0 + \alpha_1 (H/r_0)\right]\sin\theta_{\mathrm{C}}\right\}^2 \times \left\{\exp\left[(\theta - \theta_0)\tan\phi'\right]\sin\theta - \left[\sin\theta_0 + \alpha_1 (H/r_0)\right]\sin\theta_{\mathrm{C}}\right\} d\theta \\ & + \int_{\theta_{\mathrm{D}}}^{\theta_{\mathrm{h}}} \frac{\cos\theta}{\sin^3(\theta + \beta_2)} \left\{\exp\left[(\theta - \theta_0)\tan\phi'\right]\sin(\theta + \beta_2) + \exp\left[(\theta - \theta_0)\tan\phi'\right]\sin(\theta_{\mathrm{h}} + \beta_2)\right\}^2 \\ & \times \left\{\exp\left[(\theta - \theta_0)\tan\phi'\right]\sin(\theta + \beta_2) - \exp\left[(\theta - \theta_0)\tan\phi'\right]\sin(\theta_{\mathrm{h}} + \beta_2)\right\} d\theta \end{aligned} \tag{9}$$

$$\begin{aligned} f_2 = {} & \int_{\theta_0}^{\theta_{\mathrm{B}}} \frac{1}{\sin^2\theta} (\exp\left[(\theta - \theta_0)\tan\phi'\right]\sin\theta + \sin\theta_0)^2 \times (\exp\left[(\theta - \theta_0)\tan\phi'\right]\sin\theta - \sin\theta_0) d\theta \\ & + \int_{\theta_{\mathrm{B}}}^{\theta_{\mathrm{C}}} \frac{\sin\theta}{\sin^3\theta_{\mathrm{B}} \sin^3(\theta + \beta_1)} \left\{\exp\left[(\theta - \theta_0)\tan\phi'\right]\sin\theta_{\mathrm{B}} \sin(\theta + \beta_1) + \sin\theta_0 \sin(\theta_{\mathrm{B}} + \beta_1)\right\}^2 \\ & \times \left[\exp\left[(\theta - \theta_0)\tan\phi'\right]\sin\theta_{\mathrm{B}} \sin(\theta + \beta_1) - \sin\theta_0 \sin(\theta_{\mathrm{B}} + \beta_1)\right] d\theta \\ & + \int_{\theta_{\mathrm{C}}}^{\theta_{\mathrm{D}}} \frac{1}{\sin^2\theta} \left\{\exp\left[(\theta - \theta_0)\tan\phi'\right]\sin\theta + \left[\sin\theta_0 + \alpha_1 (H/r_0)\right]\sin\theta_{\mathrm{C}}\right\}^2 \times \left\{\exp\left[(\theta - \theta_0)\tan\phi'\right]\sin\theta - \left[\sin\theta_0 + \alpha_1 (H/r_0)\right]\sin\theta_{\mathrm{C}}\right\} d\theta \\ & + \int_{\theta_{\mathrm{D}}}^{\theta_{\mathrm{h}}} \frac{\sin\theta}{\sin^3(\theta + \beta_2)} \left\{\exp\left[(\theta - \theta_0)\tan\phi'\right]\sin(\theta + \beta_2) + \exp\left[(\theta - \theta_0)\tan\phi'\right]\sin(\theta_{\mathrm{h}} + \beta_2)\right\}^2 \\ & \times \left\{\exp\left[(\theta - \theta_0)\tan\phi'\right]\sin(\theta + \beta_2) - \exp\left[(\theta - \theta_0)\tan\phi'\right]\sin(\theta_{\mathrm{h}} + \beta_2)\right\} d\theta \end{aligned} \tag{10}$$

$$
\begin{aligned}
f_3 = \Bigg\{ & \sin^2\theta_0 \int_{\theta_0}^{\theta_B} \frac{\cos\theta}{\sin^3\theta}\sqrt{R^2-d_1^2}\,d\theta + \sin^2(\theta_B+\beta_1)\frac{\sin^2\theta_0}{\sin^2\theta_B}\int_{\theta_B}^{\theta_C}\frac{\cos(\theta+\beta_1)}{\sin^3(\theta+\beta_1)}\sqrt{R^2-d_2^2}\,d\theta \\
& + (\sin\theta_0 + \alpha_1 H/r_0)^2 \int_{\theta_C}^{\theta_D}\frac{\cos\theta}{\sin^3\theta}\sqrt{R^2-d_3^2}\,d\theta + \exp\left[2(\theta_h-\theta_0)\tan\phi'\right]\sin^2(\theta_h+\beta_2)\int_{\theta_D}^{\theta_h}\frac{\cos(\theta+\beta_2)}{\sin^3(\theta+\beta_2)}\sqrt{R^2-d_4^2}\,d\theta \Bigg\} \\
& + 0.5b\omega c'\cot\phi' r_0'^2 \left\{ \frac{\sin^2\theta_0\sin^2(\theta_B+\beta_1)}{\sin^2\theta_B\sin^2(\theta_C+\beta_1)} + \left[\frac{1}{\sin^2\theta_D}-\frac{1}{\sin^2\theta_C}\right](\sin\theta_0+\alpha_1 H/r_0)^2 \right. \\
& \left. + \exp\left[2(\theta_h-\theta_0)\tan\phi'\right]\left[1-\frac{\sin^2(\theta_h+\beta_2)}{\sin^2(\theta_D+\beta_2)}\right]-1 \right\}
\end{aligned}
\tag{11}
$$

## Notation

$b$: width of the insert block
$B$: total width of the mechanism
$c'$, $\phi'$: soil cohesion and internal friction angle
$d_1$, $d_2$, $d_3$, $d_4$: shortest distances between the slope and the mechanism center line
$d_p$: pile diameter
$D_c$, $D_n$: center-to-center and net intervals between neighboring piles
$D_{c'}$: work dissipation rate of soil cohesion
$D_p$: work dissipation rate of pile resistance forces
$H$: slope height
$l_p$: arm of the lateral force
$L$: projection of slope surface on horizontal plane
$L_x$: pile location
$L_{AB}$: length of line segment $AB$
$L_p$: height of piles above the slip surface
$k_{hE}$: horizontal seismic coefficient
$Q$: surcharge load
$r_0$, $r'_0$: lengths of segment OA and OA'
$r_m$: center line of the mechanism
$R$: radius of a cross section of the cone
$S_{rem}$: surface of the mechanism that exposed to air
$W_\gamma$, $W_Q$, $W_s$: work rates done by soil gravity, surcharge load and seismic force
$x_p$: parameter in Fig. 4
$z$: an arbitrary depth from the ground surface
$\alpha_1$, $\alpha_2$: depth coefficients of the upper and lower stage
$\beta_1$, $\beta_2$: inclination angles of the upper and lower stage
$\gamma$: soil unit weight
$\theta_0$, $\theta_h$: angles defining the failure mechanism configuration
$\theta_p$: polar angle corresponding to point P
$\theta_B$, $\theta_C$, $\theta_D$: polar angles corresponding to point B, C, D
$\omega$: angular velocity of the mechanism
$\lambda$: bench width coefficient